Preparation and characterization of *α*-zirconium phosphate as a perspective material for separation of ^{225}Ac and ^{213}Bi

Lukáš Ondrák[1] · Kateřina Ondrák Fialová[1] · Michal Sakmár[1] · Martin Vlk[1] · Karel Štamberg[1] · Barbora Drtinová[1] · Miroslav Šlouf[2] · Frank Bruchertseifer[3] · Alfred Morgenstern[3] · Ján Kozempel[1]

Abstract

The interest for ZrP this material is based on its physicochemical properties which makes this material a perspective candidate for applications in nuclear medicine. In this study ZrP was prepared and completely characterized using various analytical methods. Finally, the study of radiometals sorption mechanism on a surface of ZrP and the surface characterization of ZrP were done. In conclusion, ZrP appears as promising for next studies with various purposes like drug delivery system or ion-exchanger for separations of medical radionuclides such as ^{225}Ac and ^{213}Bi.

Keywords Zirconium · Phosphate · Sorption · Actinium-225 · Bismuth-213 · Drug delivery system · Ion-exchange materials

Introduction

Targeted alpha-particle therapy (TAT) is a field of nuclear medicine which uses alpha emitters to treat the oncological disease. In last years, the focus in TAT has turned on in vivo generators (e.g. ^{223}Ra, ^{225}Ac) or ^{213}Bi [1–4].

Bismuth-213 has been used in clinical trials in combination with suitable ligands for the treatment of patients with leukaemia, bladder cancer, neuroendocrine tumours, melanoma or glioma [5–9]. Due to very positive results of the clinical studies, it can be assumed that this radionuclide will establish itself in routine clinical practice once it is available in sufficient quantities and at affordable cost.

Due to its short half-life, it is convenient to obtain ^{213}Bi from an ^{225}Ac/^{213}Bi radionuclide generator [10]. A generator that has been used successfully for preclinical research and clinical application was developed at the Directorate for Nuclear Safety and Security (European Commission, Karlsruhe, Germany). This generator is based on the use of a strong organic cation exchanger AG MP-50 and is eluted with a solution of 0.1 M HCl/0.1 M NaI in ca 76% yield of ^{213}Bi, while breakthrough of the parent ^{225}Ac is below 0.2 ppm.

As obvious from the clinical trials, the ^{213}Bi use in practice is still at the very beginning, and the demand for this radionuclide may soon require large-scale production exceeding by far current availability. Therefore, it is important to look for new materials suitable in the construction of new ^{225}Ac/^{213}Bi generators, which will ensure greater yield of ^{213}Bi and possibly improve its properties (e.g. prolong its time of use due to greater radiation stability of the used sorption material).

One of the new materials for separation of ^{213}Bi from its parent ^{225}Ac could be. $Zr(HPO_4)_2 \cdot H_2O$ (ZrP). The interest in this material is based on its physicochemical properties (e.g. its extremely high ion-exchange capacity, very good biocompatibility and stability, and good thermal and radiation stability). Its properties make ZrP perspective candidate for a wide range of applications e.g. as a potentional drug delivery system or ion-exchanger [11].

✉ Lukáš Ondrák
lukas.ondrak@fjfi.cvut.cz

1 Department of Nuclear Chemistry, Faculty of Nuclear Sciences and Physical Engineering, Czech Technical University in Prague, Břehová 7, 115 19 Prague 1, Czech Republic

2 Department of Polymer Morphology, Institute of Macromolecular Chemistry, Czech Academy of Sciences, Heyrovského Nám. 2, 162 06 Prague 6, Czech Republic

3 Joint Research Centre, European Commission, Karlsruhe, Germany

Experimental

ZrP preparation

Firstly, 6.4 g of zirconium(IV) oxychloride octahydrate (Sigma-Aldrich, Germany) was dissolved in 20 ml of demineralized water. The water was demineralized using Direct-Q3 (Millipore, USA). Subsequently, 55 g of sodium dihydrogen phosphate monohydrate (Sigma-Aldrich, Germany) was dissolved in 40 ml of 3 M ultrapure hydrochloric acid (Sigma-Aldrich, Germany). Then, sodium dihydrogen phosphate monohydrate solution was added dropwise with stirring to a solution of zirconium(IV) oxychloride octahydrate at 80° C. The reaction mixture was stirred and heated using IKA C MAG HS 7.

(Sigma-Aldrich, Germany). Finally, the reaction mixture was refluxed for 30 h at this temperature. Finally, the reaction mixture was refluxed for 30 h at this temperature and then allowed to stand for two days. The precipitate was washed with 200 ml of 3 M phosphoric acid (Sigma-Aldrich, Germany) and demineralized water until pH 3 was reached [12].

ZrP characterization

The prepared ZrP was characterized using various methods to confirm its identity such as infrared spectroscopy, X-ray powder diffraction, ^{31}P NMR, thermogravimetry and differential thermal analysis and scanning and transmission electron microscopy. Finally, the characterization of the ZrP surface and the study of a metal cations sorption mechanism on ZrP were done.

Infrared spectroscopy

Infrared spectroscopy was performed using NICOLET iS50 FT-IR spectrometer, in the mid-infrared region (MIR) in the range 400–4000 cm^{-1} with a resolution of 2 cm^{-1} using ATR technique on a diamond crystal and processed in the OMNIC 9 software.

X-ray powder diffraction

X-ray powder diffraction (XRPD) analysis was performed using Rigaku MiniFlex 600 diffractometer (40 kV, 40 mA) in the range of 10–80° in Θ–2Θ geometry with a Cu-Kα1,2 X-ray tube. The ICDD PDF-2 database was used to identify the crystal phase.

Thermogravimetric (TG) and differential thermal analysis (DTA)

Thermogravimetric analysis was performed on a Labsys Evo thermogravimeter with a TG–DTA 1200 °C holder and appropriate corundum crucibles under inert gas atmosphere. The initial temperature of 20 °C was increased at the rate of 10 °C · min^{-1} to the final temperature of 800 °C.

Electron microscopy

Scanning electron microscopy

The overall morphology of the prepared nanocrystalline powder was visualized by a high-resolution field emission gun scanning electron microscopy (FEGSEM) using a microscope MAIA3 (Tescan, Czech Republic). A small amount of the nano powder was transferred to a microscopic support glass, pressed slightly by a second support glass and sputter coated with platinum (cca 4 nm layer; Vacuum sputter coater SCD 050, Leica, Austria) in order to eliminate e-beam induced charging. The sample was inserted into the FEGSEM microscope and observed by secondary electron imaging at accelerating voltage of 3 kV.

Transmission electron microscopy

The size, composition and crystal structure of nanoparticles was analysed using a Tecnai Spirit G2 transmission electron microscope (TEM; FEI, Brno, Czech Republic). The nanoparticles were deposited on a standard carbon-coated copper grid and visualized by means of bright field imaging at 120 kV. The microscope was equipped with an energy dispersive spectrometer (EDX; Mahwah, NJ, USA), which was employed in the verification of the nanoparticle elemental composition. Selected area electron diffraction mode (SAED) of the TEM microscope was used to confirm the expected crystal structure of the nanoparticles. The electron diffraction patterns were processed with ProcessDiffraction software [13] and compared with the diffraction patterns calculated with PowderCell software [14]; the expected crystal structure (α-modification of ZrP) for the diffraction pattern calculation was obtained from Crystallography Open Database [15].

### Solid-state MAS ^{31}P NMR

Solid-state MAS ^{31}P NMR cross-polarization spectra of SAMPLE. The measurement was performed at real sample temperature approx. 40 ˚C in $B_0 = 14.1$ T under 18 kHz MAS conditions with sample packed in 3.2 mm rotor. Spectra were acquired using 2 ms cross polarization from ^{1}H spin-pool with ^{1}H decoupling during direct ^{31}P FID detection.

Sorption mechanism and surface characterization

The mechanism of metal cation sorption on a surface of ZrP nanoparticles was studied using a potentiometric titration in the range of pH 2–11. ZrP (100 mg) was dispersed in 100 mL of 0.1 M NaCl (Sigma-Aldrich, Germany) to ensure ionic strength stability. The titration was performed at 25° C. The acidic part of the titration curve was measured using 1 M HCl (Sigma-Aldrich, Germany), the alkaline part of the titration curve was obtained using 0.1 M NaOH (Sigma-Aldrich, Germany). During the sample titration with 0.1 M NaOH, the sample and titrant were bubbled with gaseous nitrogen to remove CO_2 dissolved in solutions under atmospheric conditions. All titrations were repeated three time. The addition of titrant in both cases was done in steps corresponding to the volume of 0.05 ml and the pH stability condition was adjusted to 20 $mpH \cdot min^{-1}$.

The reactions taking place on the surface of ZrP can be described by three Eq. (1)-(3). The first two are protonation reactions being in progress on so-called edge-sites, SOH, the third one describes the ion-exchange on so-called layer-sites, X. This model is described in detail, e.g., in [16] and [17].

$$\equiv SO^- + H^+ \leftrightarrow SOH \tag{1}$$

$$\equiv SOH + H+ \leftrightarrow SOH_2^+ \tag{2}$$
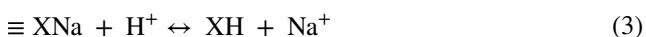
$$\equiv XNa + H^+ \leftrightarrow XH + Na^+ \tag{3}$$

The equilibrium constants for Eqs. (1)-(3), K_1, K_2 and K_{ex}, are given by Eq. (4–6):

$$K_1 = [SOH] / ([SO^-] \cdot [H^+]) \tag{4}$$

$$K_2 = [SOH_2^+] / ([SOH] \cdot [H^+]) \tag{5}$$

$$K_{ex} = ([XNa][H^+]) / ([XH] \cdot [Na^+]) \tag{6}$$

Protonation and sorption processes taking part on the edge sites can be described by several types of Surface Complexation Models (SCM) [15, 16] from which the following ones are most utilized: Constant Capacitance Model (CCM), Diffusion Double Layer Model (DLM) and non-electrostatic Chemical Equilibrium Model (CEM). The processes taking part on layer sites are always described by classical Ion Exchange Model (IExM). It is to be noted that the key assumption of surface models is the validity of Boltzman Eq. (7) [14] quantifying the relation between the concentration of ith-component in a aqueous phase near the surface, $(C_i)_S$, and its bulk concentration, C_i:

$$(C_i)_s = e^{\left(-\frac{z \cdot \psi \cdot F}{R \cdot T}\right)}, \tag{7}$$

where z is the charge of ith-component, ψ [V] is the electrostatic potential, F [$C \cdot mol^{-1}$] is Faraday constant, R [$J \cdot K^{-1} \cdot mol^{-1}$] is the gas constant and T [K] is the absolute temperature.

The above given equations allow us to deduce relationship between surface charge σ [$C \cdot m^{-2}$] and electrostatic potential ψ providing Eq. (8)-(10):

$$\sigma = G \cdot \psi \text{ (CCM model)} \tag{8}$$

$$\sigma = 0.1174 \cdot I^{1/2} \cdot \sinh\left(\frac{z_i \cdot \psi \cdot F}{2 \cdot R \cdot T}\right) \text{ (DLM model)} \tag{9}$$

$$\psi = 0 \; (C_i)_S = C_i \text{ (CEM model)}, \tag{10}$$

where G [$F \cdot m^{-2}$] is so called Helmholtz capacitance.

The titration curves of ZrP were evaluated using the software product FAMULUS and the proper code P46DN-RLG.fm (code package STAMB 2015). The Newton–Raphson multidimensional nonlinear regression procedure and WSOS/DF as the criterion of goodness-of-fit were used [16].

Results and discussion

Infrared spectroscopy

In the measured spectrum (see Fig. 1) there are two bands at approx. 3590 and 3140 cm^{-1} belonging to the asymmetric stretching vibration of the intercalated molecules
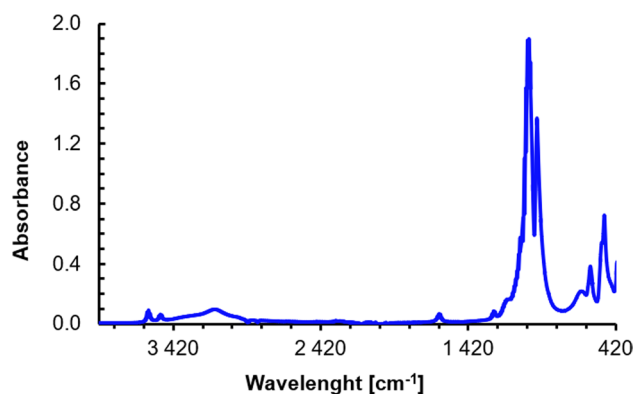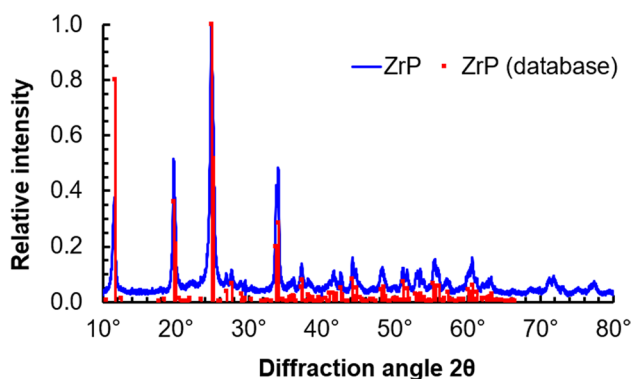

Fig. 1 FT-IR spectrum of prepared ZrP

Fig. 2 XRPD analysis of prepared ZrP

Fig. 3 TG and DTA analysis of prepared ZrP

of crystalline water. The band at 1620 cm^{-1} belongs to the deformation vibrations of bonds in the OH^{-} groups presented in molecules of water. Next band appeared at approx. 1250 cm^{-1} represents out-of-plane bending vibrations of P-OH group. The most intensive band at approx. 1015 cm^{-1} might be attributed to the stretching vibration of $(PO_4)^{3-}$ group. Complementary bands to this band are being visible at 594 resp. 515 cm^{-1} and belongs to the deformation vibrations of the $(PO_4)^{3-}$ group.

X-ray powder diffraction

The result of X-ray powder diffraction (XRPD) analysis is shown in Fig. 2, where the measured diffractogram is compared with a library data, which indicates the presence of α modification of ZrP.

The main three diffraction peaks at approx. 12°, 20° and 25° corresponding with the characteristic diffraction peaks of d (002), d (110) and d (112) respectively.

The monoclinic crystallisation system (P21/n space group) was also confirmed using XRPD.

Thermogravimetric (TG) and differential thermal analysis (DTA)

The presence of free and crystalline water was also confirmed by the results of thermogravimetric analysis shown in Fig. 3. The TG curve shows the first more significant change in weight corresponding to about 6% at a temperature of 100 ˚C, when the free water evaporates and the α-Zr(HPO$_4$)$_2$ is formed. The second loss of 6%

of weight is observed at the temperature about 600 °C which is associated with dehydration condensation reaction of P-OH groups of created α-Zr(HPO$_4$)$_2$ and loss of crystalline water resulted in a formation of ZrP$_2$O$_7$. The processes described above were confirmed also with the shape of DTA curve where the exothermic nature of the ongoing reaction of free or crystalline water loss can be seen.

Electron microscopy

Figure 4 summarizes the results of the electron microscopy analysis of the prepared crystalline nanoparticles of ZrP. The average size of the nanocrystals was approximately 150 nm as demonstrated by both secondary electron imaging in FEGSEM microscope (FEGSEM/SE; Fig. 4a) and bright field imaging in TEM microscope (TEM/BF; Fig. 4b). Selected-area electron diffraction pattern (TEM/SAED; inset in Fig. 4b) proved that the particles are crystalline. A comparison of the radially averaged experimental TEM/SAED pattern with the theoretically calculated powder X-ray diffraction pattern (PXRD) of α-ZrP Fig. 4c) confirmed the expected crystal structure, i.e. the alpha crystalline modification of ZrP. Elemental analysis (TEM/EDX; Fig. 4d) confirmed the electron diffraction results: Except for the peaks corresponding to carbon-coated copper grid (C, Cu), the most intense peaks in EDX spectrum (Zr, P and O) corresponded to the composition of the prepared nanocrystals. Small silicon peak of silicon at 1.74 keV could be attributed to the fluorescence from the Si-detector [18].
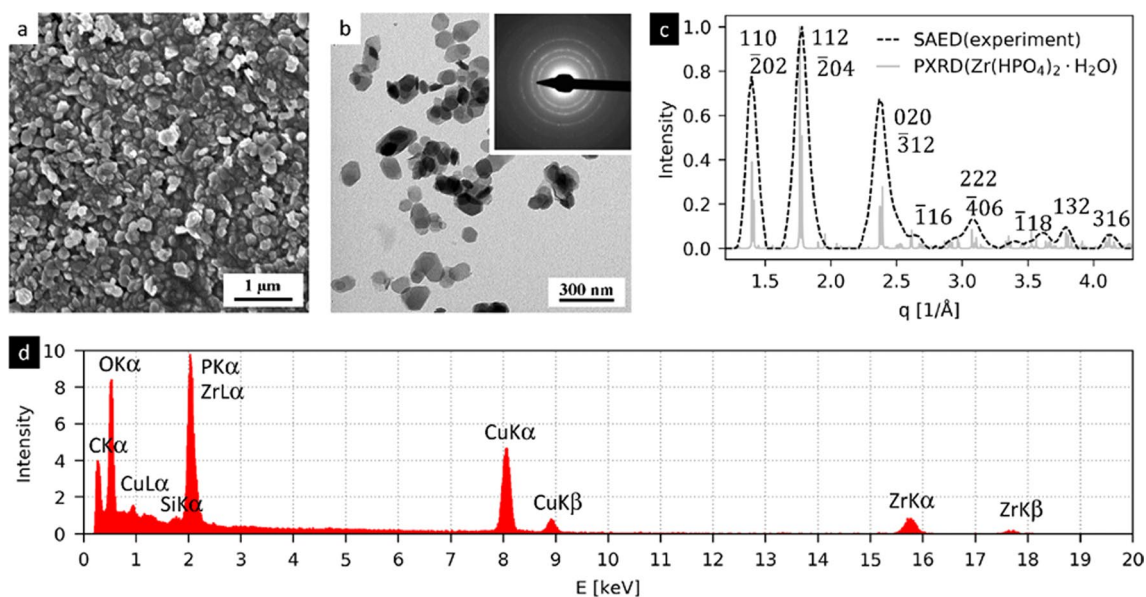
Fig. 4 Electron microscopy analysis of the morphology, crystal structure and elemental composition of the prepared nanocrystals: **a** FEGSEM/SE analysis, **b** TEM/BF analysis, **c** comparison of the experimental TEM/SAED pattern with theoretically calculated X-ray diffraction pattern (PXRD), and **d** energy-dispersive spectrum (TEM/EDX) of the nanocrystals
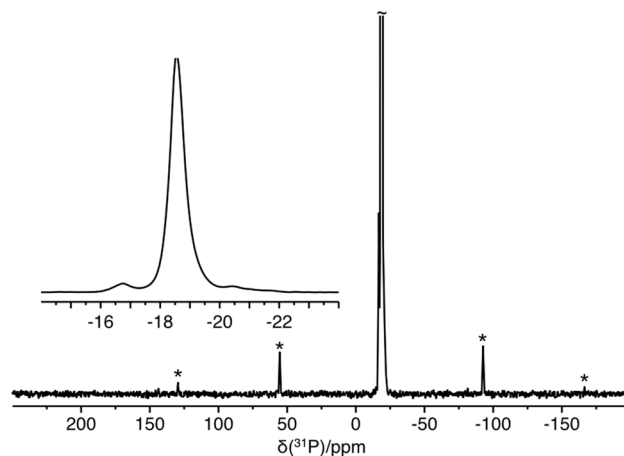
Solid-state MAS ^{31}P NMR

The measured ^{31}P solid-state NMR spectrum (see Fig. 5) contains one major signal accompanied with two signals with very low intensity. The position of the major signal is in the chemical-shift region typical for phosphates. The single major peak in the spectrum confirms the polymorphic purity of the sample.

Sorption mechanism and surface characterization

Values of WSOS/DF, of equilibrium constants K_1, K_2, K_{ex}, and of total concentration on the edge sites, ΣSOH, and on the layer sites, ΣX, were deduced from the titration curves. The results are summarised in Table 1 and displayed in Figs. 5 and 6.

According to the WSOS/DF values, there is no difference between the individual models. However, if we consider the values of individual quantities, the CEM model seems to be the most plausible, being followed by the

Fig. 5 Solid-state MAS ^{31}P NMR cross-polarization spectra of prepared ZrP. Asterisks indicate rotational sidebands

DLM model. For this reason, these two models are shown in Figs. 6 and 7.

Figure 6 and 7 show the results of a good fit of the experimental data and also show the representation of

Table 1 Resulting values of quantities obtained in the course of evaluation of titration data

Model	ΣSOH [mol·kg^{-1}]	ΣX [mol·kg^{-1}]	K_1 [L·mol^{-1}]	K_2 [L·mol^{-1}]	K_{ex} [−]	WSOS/DF
CEM+IExM	2.14±0.20	4.62±0.23	$5.36\cdot10^7\pm3.04\cdot10^7$	$2.93\cdot10^5\pm2.07\cdot10^5$	32.00±7.56	0.44
CCM+IExM	6.50±1.29	~7.35	$5.73\cdot10^{21}\pm3.50\cdot10^{10}$	$9.16\cdot10^8\pm7.56\cdot10^8$	5.55±3.24	0.41
DLM+IExM	4.22±0.56	6.75±0.59	$3.57\cdot10^{13}\pm15.410^{13}$	$3.60\cdot10^{11}\pm3.55\cdot10^{11}$	20.30±4.74	0.76
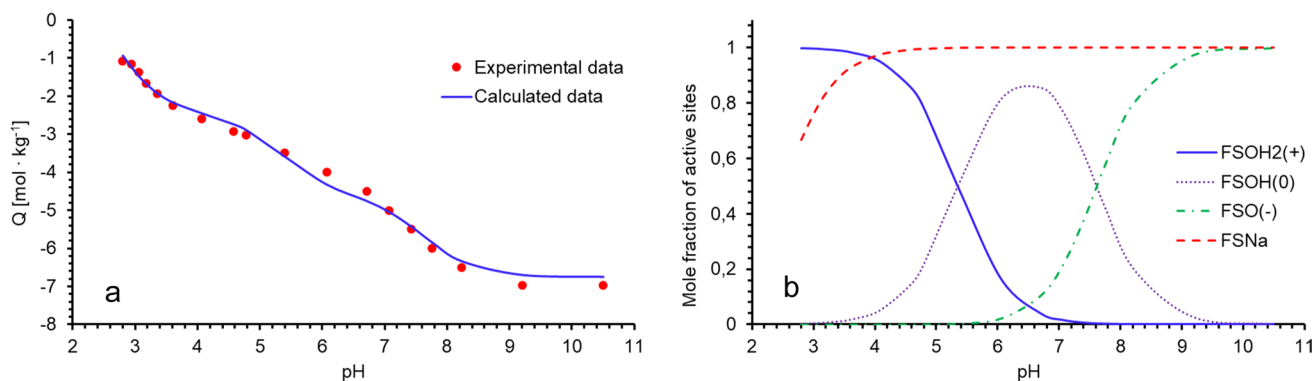
Fig. 6 The evaluation of experimental titration curve by means of CEM + IExM models: **a** experimental and calculated titration curve, **b** molar fractions of surface sites individual forms
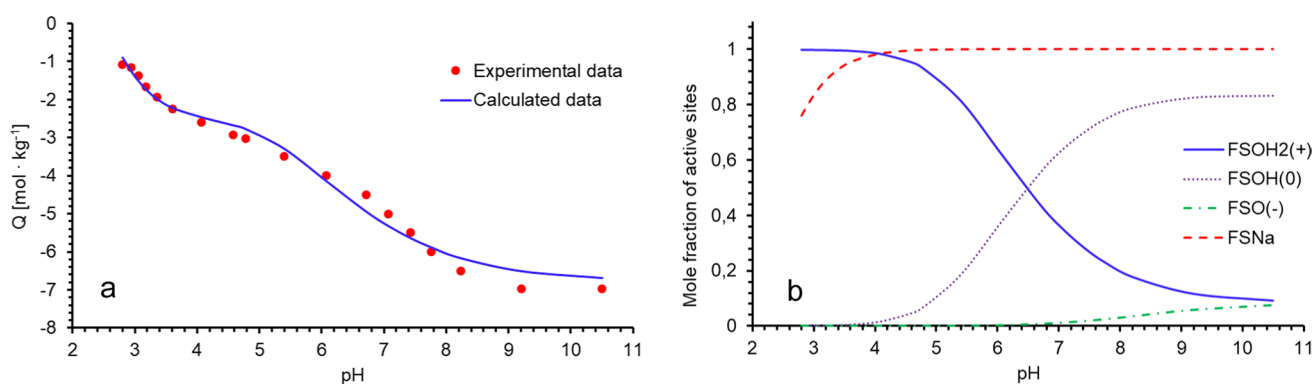
Fig. 7 The evaluation of experimental titration curve by means of DLM + IExM models: **a** experimental and calculated titration curve, **b** molar fractions of surface sites individual forms

the individual surface groups. It is obvious that the fit is very good and that the groups with a negative charge, i.e. FSO⁻ on which cation exchange potentially takes place, clearly predominate. In comparison with the titration results of nano-TiO$_2$.xH$_2$O [16], the ZrP titration curve is placed in the region with a predominant negative surface charge. ZrP has also orders of magnitude higher total concentrations of ΣSOH and ΣX, which indicates potentially higher sorption capacity, especially in cationic forms. From this point of view, the ZrP sorbent seems to be promising for the intended application.

Conclusions

The novel promising material for separation of new promising alpha emitting therapeutical radionuclides such as ²²⁵Ac and ²¹³Bi and as well as material for novel types of drug delivery system of alpha emitters, α-ZrP, was prepared, completely characterised and a sorption mechanism on the surface of this material and its surface characteristics were

evaluated. The titration curve of ZrP appears in an area with a predominant negative charge. ZrP evinces high concentration of functional groups for cation sorption, indicating thus potentially high sorption capacity. From this point of view, ZrP urges for further investigation of its suitability for drug delivery systems or ion-exchange material for separation of medically relevant radionuclides such as ²²⁵Ac and ²¹³Bi. Our next aim is evaluating sorption properties of ZrP in various conditions, particularly the ²²⁵Ac sorption kinetics.

Declarations

Conflict of interest The authors declare no conflict of interest.

References

1. Jurcic JG (2018) Clinical studies with Bismuth-213 and Actinium-225 for hematologic malignancies. Curr Radiopharm 11:192–199
2. Nilsson S, Larsen RH, Fossa SD et al (2005) Clinical experience with α-emitting radium-223 in the treatment of skeletal metastases. Clin Cancer Res 12:4451–4459
3. Carrasquillo JA, O'Donoghue JA, Pandit-Taskar N et al (2013) Phase I pharmacokinetic and biodistribution study with escalating doses of ^{223}Ra-dichloride in men with castration-resistant metastatic prostate cancer. Eur J Nucl Med Mol Imaging 40:1384–1393
4. Sgouros G, Ballangrud AM, Jurcic JG et al (1999) Pharmacokinetics and dosimetry of an α-particle emitter labelled antibody: ^{213}Bi-HuM195 (Anti-CD33) in patients with leukemia. J Nucl Med 40:1935–1946
5. Jurcic JG, Larson SM, Sgouros G et al (2002) Targeted α particle immunotherapy for myeloid leukemia. Blood 100:1233–1239
6. Autenrieth ME, Seidl Ch, Bruchertseifer F et al (2018) Treatment of carcinoma in situ of the urinary bladder with an alpha-emitter immunoconjugate targeting the epidermal growth factor receptor: a pilot study. Eur J Nucl Med 45:1364–1371
7. Kratochwil C, Giesel FL, Bruchertseifer F et al (2014) ^{213}Bi-DOTATOC receptor-targeted alpha-radionuclide therapy induces remission in neuroendocrine tumours refractory to beta radiation: a first-in-human experience Eur. J Nucl Med 41:2106–2119
8. Allen BJ, Raja Ch, Rizvi S et al (2005) Intralesional targeted alpha therapy for metastatic melanoma. Cancer Biol Ther 4:1318–1324
9. Kneifel S, Cordier D, Good S et al (2006) Local targeting of malignant gliomas by the diffusible peptidic vector 1,4,7,10-tetraaza-cyclododecane-1-glutaric acid-4,7,10-triacetic acid-substance *p*. Clin Cancer Res 12:3843–3850
10. Morgenstern A, Apostolidis Ch, Kratochwil C et al (2018) An overview of targeted alpha therapy with ^{225}Actinium and ^{213}Bismuth. Curr Radiopharm 11:200–208
11. Xiao H, Liu S (2018) Zirconium phosphate (ZrP)-based functional materials: synthesis, properties and applications. Mater Des 155:19–35
12. Wiikinkoski EW, Harjula RO, Lehto JK et al (2017) Effects of synthesis conditions on ion exchange properties of α-zirconium phosphate for Eu and Am. Radiochim Acta 105:1033–1042
13. Labar JL (2005) Consistent indexing of a (set of) SAED pattern(s) with the process diffraction program. Ultramicroscopy 103:237–249
14. Kraus W, Nolze G (1996) POWDER CELL - a program for the representation and manipulation of crystal structures and calculation of the resulting X-ray powder patterns. J Appl Cryst 29:301–303
15. Grazulis S, Chateigner D, Downs RT et al (2009) Crystallography open database-an open-access collection of crystal structures. J Appl Cryst 42:726–729
16. Kukleva E, Suchánková P, Štamberg K et al (2019) The determination of parameters characterizing the surface protolysis properties of nano-HAp and nano-TiO$_2$ by means of titration method. RSC Adv 9:21989–21995
17. Filipská H, Štamberg K (2005) Mathematical modelling of a Cs(I)-Sr(II)-bentonite-magnetite sorption system simulating the processes taking place in deep geological repository. Acta Polytech 45:11–18
18. Williams DB (2009) Transmission electron microscopy, 2nd edn. Springer, New York

Publisher's Note Springer Nature remains neutral with regard to jurisdictional claims in published maps and institutional affiliations.